Simulating the filament morphology in electrochemical metallization cells

NEUROMORPHIC
Computing and Engineering

OPEN ACCESS

RECEIVED
3 January 2023

REVISED
31 May 2023

ACCEPTED FOR PUBLICATION
6 June 2023

PUBLISHED
21 June 2023

PAPER

Simulating the filament morphology in electrochemical metallization cells

Milan Buttberg[1], **Ilia Valov**[1,2] **and Stephan Menzel**[1,2,*]

[1] Institute of Materials in Electrical Engineering and Information Technology II, RWTH Aachen University, Sommerfeldstraße 24, 52074 Aachen, Germany
[2] Forschungszentrum Jülich GmbH, Peter Grünberg Institute (PGI 7) and JARA-FIT, Wilhelm-Johnen-Straße, 52428 Jülich, Germany
* Author to whom any correspondence should be addressed.

E-mail: st.menzel@fz-juelich.de

Keywords: ECM, CBRAM, conductive filament, continuum simulation, ReRAM, memristive device, electrochemical metallization

Abstract

Electrochemical metallization (ECM) cells are based on the principle of voltage controlled formation or dissolution of a nanometer-thin metallic conductive filament (CF) between two electrodes separated by an insulating material, e.g. an oxide. The lifetime of the CF depends on factors such as materials and biasing. Depending on the lifetime of the CF—from microseconds to years—ECM cells show promising properties for use in neuromorphic circuits, for in-memory computing, or as selectors and memory cells in storage applications. For enabling those technologies with ECM cells, the lifetime of the CF has to be controlled. As various authors connect the lifetime with the morphology of the CF, the key parameters for CF formation have to be identified. In this work, we present a 2D axisymmetric physical continuum model that describes the kinetics of volatile and non-volatile ECM cells, as well as the morphology of the CF. It is shown that the morphology depends on both the amplitude of the applied voltage signal and CF-growth induced mechanical stress within the oxide layer. The model is validated with previously published kinetic measurements of non-volatile Ag/SiO_2/Pt and volatile Ag/HfO_2/Pt cells and the simulated CF morphologies are consistent with previous experimental CF observations.

1. Introduction

Resistive memory cells have promising potential for emerging technologies such as neuromorphic computing, but also for established memory applications [1]. One type of resistive memory cells is electrochemical metallization (ECM) cells, also known as conductive bridge random access memory cells [2–4]. This two-terminal device can be described as a nano-capacitor-like structure. The counter electrode (CE) consists of an inert metal, such as Pt or W, whereas the active electrode (AE)—typically Ag, Cu or Ni—is electrochemically soluble in the nanometer-thin, sufficient ion-conducting switching layer (SL), which separates the metallic electrodes [5–7]. For the SL different materials were reported: metal oxides [8], chalcogenides [9], 2D materials like h-BN [10] and even organic materials [11]. Applying a positive bias to the AE leads to the oxidation of the AE and incorporation of cations from the AE/SL interface into the SL. After formation of a critical nucleus at the CE, the cations start preferably reduce at the nucleus. The so formed metallic pathway, called conductive filament (CF), grows into the SL and into the direction of the AE. The CF can either short circuit both electrodes, or a nanometer wide gap remains between the CF and one of the electrodes, enabling the flow of electronic tunneling currents [6, 12]. Formation of a quantum point contact is also possible [13–15]. The CF reduces the resistance of the device and therefore this effect is called SET. In non-volatile ECM cells the CF is stable and negative bias reverses the processes, leading to rupture of the CF; the system now is in the high resistive state after a so called RESET [16]. In volatile ECM cells the CF is unstable and has a low retention [17]; authors propose a surface diffusion mechanism, leading to self-relaxation of the CF [18]. Both effects, namely RESET by electrical stimulus and self-relaxation, have been observed in the same device depending on the maximum current during the SET. In general, the lifetime

of a CF in volatile and non-volatile ECM cells can range from microseconds to years. The lifetime plays a crucial role for the usage in applications and has to be engineered with high precision. For brain-inspired neuromorphic applications, non-volatile ECM cells mimic synaptic behavior [19–21], while volatile ECM cells can be used as integrate-and-fire neurons [21, 22]. In storage applications, volatile ECM cells are used as selectors in crossbar arrays, while for the memory itself a non-volatile ECM is required with retention of ten years [23, 24]. To enable such technologies, filament lifetime control is critical. Many authors link the lifetime of the CF to its morphology, more precisely, the radius of the CF [18, 24–27]. Various experiments observe a wide variety of morphologies in this regard: bulky and directed, cone-shaped, reverse cone-shaped, hourglass-shaped, thin and wire-like and dendritic [20, 28–35]. For simplification, these morphologies are often predefined in simulations [25, 36, 37]. Continuum models tend to result into conical or also cylindrical morphologies [5, 18, 38, 39]. Kinetic Monte Carlo (KMC) models, on the other hand, show dendritic to bulky CFs, depending on the applied voltage, where higher voltage leads to thinner filaments [40–42]. Some authors also propose self-induced mechanical stress on the CF due to compression of the surrounding host matrix [41, 43]. Implemented into a KMC model, mechanical stress leads to even more laterally constraint CF morphologies [41]. However, the big disadvantage of KMC models is the computational effort and the associated long computing time. To improve the development of ECM cell technologies, there is a need for continuum models that account for all relevant physical effects and are capable of simulating CF morphology for various applied voltages to explain self-relaxation and retention observations.

In this work, a 2D axisymmetric continuum model for ECM devices without predefined filament morphology is reported and mechanical stress is introduced within the SL. Mechanical stress provides an energy barrier that hinders the reduction of cations in lateral direction and thus effectively limits the lateral growth of the CF. It is shown that the radial dimension of the CF is a function of applied voltage, mechanical stress and the ion conducting properties of the SL. Thus, this model is capable of reproducing most observed filament morphologies. The influence of aforementioned parameters is investigated and the simulation results are compared with reported kinetic measurements from non-volatile Ag/SiO_2 (10 nm)/Pt devices and volatile Ag/HfO_2 (3 nm)/Pt devices.

2. Physical model

2.1. Equation system for ECM type switching

Our 2D axisymmetric continuum model contains of three layers, an active Ag top electrode (AE), a solid ion conductor, also called SL and an inert Pt CE. A fourth layer on top of the three-layer cell stack models a linear series resistor R_L to limit the maximum current through the cell. Four different growth modes have been reported for CF growth in ECM cells depending on high or low active ion mobility and ion injection, respectively [44]. In this work only two growth modes are simulated, namely the growth modes with high ion mobility and high or low ion injection rate. Both growth modes lead to CF formation on the CE. Thus, the critical nucleus is placed on the CE and it is assumed that a critical nucleus already formed at the SL/CE interface. The other two growth modes would require the modeling of nucleation within the SL and the modeling of the redox reactions at the resulting clusters (which act as bipolar electrodes). The nucleus is modeled by a quadrant of a circle at the CE/SL interface at the symmetric axis. The size of the nucleus is comparable to the size of a metal atom. The continuum modeling of ECM cells is linked to several requirements. Overall, it is assumed that forming has already occurred and thus all simulated events are after it. Furthermore, it is assumed that the CF completely dissolves after a RESET or due to the volatility of the cell stack and that a new nucleus must form in each subsequent SET event. Kinetic measurements on the simulated cell stacks show different slopes. In fact, the slope at low voltages corresponds to the nucleation limitation. Thus, each SET event starts with a nucleation and not with a remnant CF.

Further, a voltage jump should occur at the metal–insulator interfaces, which represents the overpotential of an electrochemical reaction. Furthermore, it is assumed that there is no accumulation of charge. These requirements can be fulfilled by coupling two Laplace equations. A first Laplace equation models the electric field distribution in the metallic domains (figure 1, domains R_L, AE, critical nucleus/CF, CE):

$$\sigma_{\mathrm{me}} \Delta V_1 = 0. \tag{1}$$

A second Laplace equation accounts for the solid electrolyte (figure 1, domain SL) [5]:

$$\sigma_{\mathrm{ion}} \Delta V_2 = 0. \tag{2}$$

The coupling by means of Neumann boundary conditions—defined later—leads to a voltage jump at the interfaces with continuous current. The potentials in the metallic domains are denoted as $V_1(r,z)$ and in the SL as V_2 (r,z), respectively. The electric and ionic conductivities are denoted as σ_{me} and σ_{ion}, respectively.

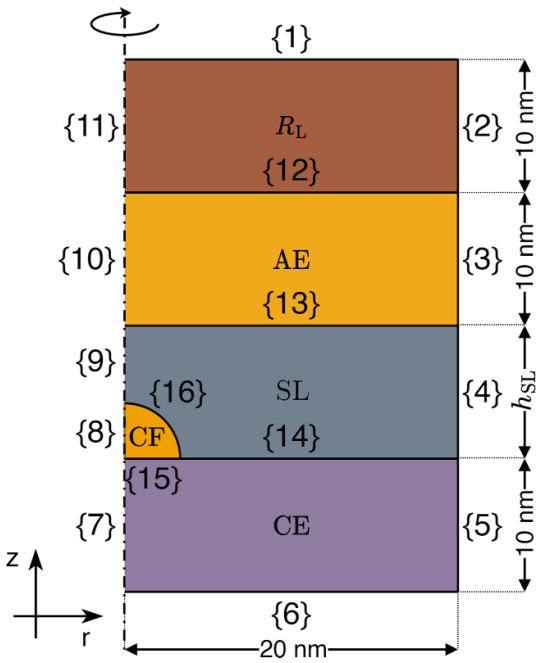

Figure 1. Simulation geometry with boundary numbering, active electrode AE, counter electrode CE, switching layer SL, overdrawn critical nucleus/CF and load resistor R_L. Boundary numbering is used to connect boundaries to boundary conditions. Applied voltage and ground are applied on boundaries {1} and {6}, zero flux is applied on boundaries {2}–{5} and {7}–{11}. Moving mesh boundary conditions are applied on boundaries {8}, {9} and {13}–{16}.

While the conduction mechanism in the metallic domains is purely electronic, an ionic conduction mechanism is assumed in the SL, namely ion hopping induced by an electric field. The Mott–Gurney law is used to describe the oxide conductivity as

$$\sigma_{\text{ion}} = 2z_c e c_{\text{ion}} f_{\text{hop}} a_{\text{hop}} \exp\left(\frac{-\Delta G_{\text{hop}}}{k_B T}\right) \sin h\left(\frac{a_{\text{hop}} z_c e}{2k_B T}\vec{E}\right)\vec{E}^{-1} \tag{3}$$

with the ion charge number z_c, elemental charge e, the ion concentration c_{ion}, the attempt frequency f_{hop}, the hopping distance a_{hop}, the Boltzmann constant k_B, the temperature T, the hopping energy ΔG_{hop}, and the local electric field $\vec{E}$ [45, 46]. The resulting current from the electrochemical reactions at the AE/SL, CF/SL and CE/SL interfaces are calculated using the Butler–Volmer equation [47, 48]:

$$J_{\text{BV}} = J_0\left\{\exp\left(\frac{(1-\alpha)z_c e}{k_B T}\Delta\varphi\right) - \exp\left(-\frac{\alpha z_c e}{k_B T}\Delta\varphi\right)\right\} \tag{4}$$

with the charge transfer coefficient α, the overpotential η and the exchange current density J_0 which can be expressed as

$$J_0 = z_c e c_{\text{ion}} k_0 \exp\left(-\frac{\Delta W_A}{k_B T}\right) \tag{5}$$

with the ion concentration c_{ion}, the heterogeneous rate constant k_0 and the activation energy ΔW_A [48]. For nanometer-thin SLs or a grown CF with a nanometer wide gap to the TE, electronic tunneling currents occur. For an applied voltage $|V| > 0 \wedge e \cdot |V| \ll \Delta W_0$, with the tunnel barrier height ΔW_0, a trapezoidal barrier is assumed, which is modeled using the voltage–current relation derived by Simmons [49, 50]. Thus,

$$J_{\text{Tu}} = \frac{\sqrt{2m_r \Delta W_0}}{2\Delta z}\left(\frac{e}{h}\right)^2 \exp\left(-\frac{4\pi\Delta z}{h}\sqrt{2m_r \Delta W_0}\right) V_{\text{Tu}}, \tag{6}$$

with the gap Δz, the tunnel voltage V_{Tu} between CF and AE, the Planck's constant h, and the effective electron mass m_r.

Figure 1 shows the simulation geometry with the numbered boundaries which will be referenced to following boundary conditions and specified in curly braces. The CE {6} is set to ground level, while the

linear series resistor R_L {1} is biased with a rectangular voltage signal V_{app}. Neumann boundary conditions couple equations (1) and (2) at the metallic-ion-conducting interfaces {13, 14, 16}. Hence,

$$nJ_1 = -J_{BV} - J_{Tu} \tag{7}$$

for equation (1) and

$$nJ_2 = J_{BV} \tag{8}$$

for equation (2), both on boundaries {13}, {14} and {16} [5, 51]. Simmons electron tunneling only occurs between CF {16} and AE {13} and is set to zero for transitions between CE {14} and AE {13}. Ionic currents occur within the SL and are coupled to the metallic domains with equation (4). The outer boundaries {2, 3, 4, 5} as well as the symmetric axis have zero flux. Note that the CF domain in figure 1 is exaggerated for $t = 0$.

For a CF to form and grow, first there has to form a critical nucleus at the CE. At this critical nucleus the reduction of AE ions takes place preferably, leading to CF growth. The time for a critical nucleus to form, called nucleation time, is calculated according to

$$t_{nuc} = t_{0,nuc} \exp\left(\frac{\Delta G_{nuc}^{\neq}}{k_B T}\right) \exp\left(-\frac{(N_c + \alpha_{nuc}) z_c e}{k_B T} \Delta\varphi_{nuc}\right), \tag{9}$$

with the prefactor $t_{0,nuc}$, the activation energy $\Delta G_{nuc}^{\neq}$, the number of atoms N_C in the critical nucleus, the charge transfer coefficient α_{nuc} during nucleation and the overpotential $\Delta\varphi_{nuc}$. Before t_{nuc} is reached, the CF growth is inhibited [52]. The filament growth at the CE is described using Faradays Law [47]:

$$\frac{\partial n}{\partial t} = -\frac{M_{AE}}{z_c e \rho_{AE}} J_{BV} \tag{10}$$

where ∂n is the normal of CF growth, M_{AE} the molar mass of the AE material, and ρ_{AE} the density of the AE material. For CF growth, a moving mesh applies to the CF/SL interface {16} with equation (10) as normal velocity boundary condition. The deformation of boundaries not adjacent to the CF is set to zero {1–7, 10–13}. For boundaries {8} and {9}, lateral deformation is set to zero to allow vertical deformation as the filament grows. For boundaries {14} and {15} vertical deformation is set to zero accordingly and lateral growth is allowed. The moving mesh distorts the mesh, which makes re-meshing necessary. Re-meshing takes place when a specific distortion threshold of the mesh is reached. A new geometry is created, the old solution is projected onto the new mesh and the calculations continue. A triangular mesh is used.

The maximum current through the device should be limited to avoid thermal breakdown after a SET transition [53, 54]. This is achieved by using an additional resistive layer on top of the AE with linear resistance behavior, thus modeling a series resistor as often used in measurements. The specific conductivity σ_{RL} of the resistive layer is calculated depending on the desired resistor value. For this study, a value of $R_L = 1\,\mathrm{M\Omega}$ has been chosen. Thus σ_{RL} can be written with the well-known formula for the specific conductivity as

$$\sigma_{RL} = R^{-1} \cdot h_{RL} {w_{cell}}^{-2} \pi^{-1} \tag{11}$$

with the length of the resistor h_{RL} and its cross-sectional area $\pi {w_{cell}}^2$. Tables 1 and 2 show the simulation parameters for the two investigated cell stacks, namely Ag/SiO_2/Pt and Ag/HfO_2/Pt, respectively. For the analysis of the SET kinetics thermal effects can be neglected as the currents during growth are too low ($\ll 1\ \mu$A) to generate relevant Joule heating. In addition, Ag is a very good heat conductor dissipating the heat efficiently. The commercial software COMSOL and MATLAB were used for all simulations.

2.2. Mechanical stress

To include the influence of mechanical stress, the set of equations defined so far is modified. Various studies have shown the influence of mechanical stress on the switching behavior and filament morphology in ECM cells [41, 43]. It is assumed that in the SL a nanotemplate with radius r_{tem} already exists, where the filament grows preferentially. Causes for this can be electroforming, amorphous microfilms, grain boundaries, dislocations, (lattice) defects and electrode interfaces. To model the mechanical stress, a modified model from [41] was used by setting the mechanical work inside the nanotemplate to zero. This allows to simulate nanotemplates of different radii. Hence,

$$\Delta W_{mech}(r) = 0 \quad \text{for } r < r_{tem} \tag{12}$$

Table 1. Simulation model parameters $Ag/SiO_2/Pt$ cell.

Symbol	Value	Symbol	Value	Symbol	Value
ΔW_A	0.55 eV	ΔW_{hop}	0.3 eV	c_{ion}	8×10^{25} m^{-3}
z_c	1	α	0.84	N_c	1
m_r	0.84	ρ_{Ag}	1.7×10^{-8} Ωm	α_{nuc}	0.32
ΔW_0	2.7 eV	ρ_{Pt}	1.1×10^{-7} Ωm	k_0	2×10^5 ms^{-1}
T	298 K	$\Delta G^{\neq}_{nuc}$	0.8 eV	Y	100 GPa
f_{hop}	1×10^{14} Hz	$t_{0,nuc}$	1×10^{-8} s	M_{Ag}	107.87 gmol^{-1}
a_{hop}	0.3 nm	h_{SL}	10 nm	σ_{RL}	7.957 Sm^{-1}
h_{ME}	10 nm	h_{RL}	10 nm	w_{cell}	20 nm

Table 2. Simulation model parameters $Ag/HfO_2/Pt$ cell.

Symbol	Value	Symbol	Value	Symbol	Value
ΔW_A	0.62 eV	ΔW_{hop}	0.18 eV	c_{ion}	3×10^{26} m^{-3}
z_c	1	α	0.84	N_c	1
m_r	0.15	ρ_{Ag}	1.7×10^{-8} Ωm	α_{nuc}	0.32
ΔW_0	2.7 eV	ρ_{Pt}	1.1×10^{-7} Ωm	k_0	3×10^7 ms^{-1}
T	298 K	$\Delta G^{\neq}_{nuc}$	0.8 eV	Y	180 GPa
f_{hop}	1×10^{14} Hz	$t_{0,nuc}$	1×10^{-8} s	M_{Ag}	107.87 gmol^{-1}
a_{hop}	0.3 nm	h_{SL}	3 nm	σ_{RL}	7.957 Sm^{-1}
h_{ME}	10 nm	h_{RL}	10 nm	w_{cell}	20 nm

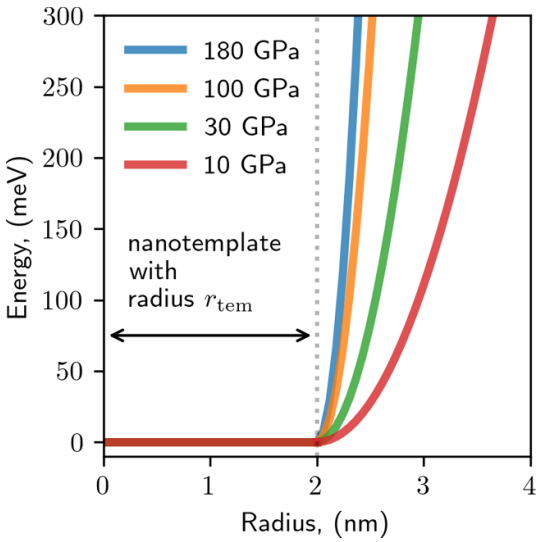

Figure 2. Mechanical work for different Young's moduli of the host matrix. A nanotemplate of 2 nm was considered as an example to illustrate the mechanical stress model. It is postulated that the CF preferably grows within the nanotemplate.

$$\Delta W_{mech}(r) = \frac{YA}{w_{cell}} \int (r - r_{fil})\, dr \quad \text{for } r \geqslant r_{tem}, \tag{13}$$

with Y the Young's modulus of the SL, A the cross-sectional area of an active ion, w_{cell} the width of the simulated cell and r the radial distance from the symmetric axis. As proposed in [41], this additional energy is added to the activation energy for a reduction, which changes ΔW_A in equation (5) to an effective energy $\Delta W_{A,eff} = \Delta W_A + \Delta W_{mech}$. Figure 2 exemplarily shows the additional mechanical work as function of the filament radius. A nanotemplate radius $r_{tem} = 2$ nm was assumed and the resulting curves for different plausible Young's moduli are plotted. For the Young's modulus of SiO_2, various values have been reported in literature, from $10 - 40$ GPa [55], up to 100 GPa [56]. For thin film HfO_2 values up to 180 GPa have been reported [57]. The size of the nanotemplate can be set to different values and, as will be discussed later, this parameter is critical for the morphology of the filament.

3. Results and discussion

3.1. Switching kinetics and filament morphology

A crucial parameter for ECM cell operation is the switching time t_{SET}, which is defined as the time for a transition from high resistive state (HRS) to low resistive state (LRS) during constant bias. For varying bias, t_{SET} changes over orders of magnitudes in time, resulting in the well-known SET kinetics with exponential dependence of the switching time on the applied voltage. Various authors have identified three different rate-determining regimes [58–62] which all have been introduced above by equations (3)–(9). For low voltages the formation of a critical nucleus is rate determining. For intermediate voltage ranges the electron-transfer reactions at the metal–isolator interfaces lead to further limitation. For high voltages, the limitation comes from a combination of electron-transfer reactions and ion drift. In this regime, also the RC-time of parasitic capacitances can lead to a limitation [63].

In this study, we conduct pulse simulations to investigate not only the switching time, but also the morphology of the CF and its evolution over time. The model is tested using two different kinetic data sets, one from measurements of non-volatile Ag/SiO_2/Pt cells, and the other one from volatile Ag/HfO_2/Pt cells. For the investigated Ag/HfO_2/Pt stack, no VCM-type of forming is observed as the device returns to its initial as-deposited resistance after relaxation/RESET [26]. Both cells use Ag as the AE and Pt as CE. The SL is SiO_2 ($h_{SL} = 10$ nm) and HfO_2 ($h_{SL} = 3$ nm), respectively. Tables 1 and 2 show the simulation parameters for the SiO_2 and the HfO_2 cell stack, respectively [26, 64]. One set of simulations is defined as different simulations at different voltages, namely from 0.2 V to 2.5 V for the SiO_2 stack and 0.4 V to 2.2 V for the HfO_2 stack. The simulations are aborted when a CF reaches 97% of the SL height h_{ox}. For the kinetic curves, the SET time t_{SET} is extracted and plotted against the applied voltage. Figure 3 shows the experimental data for both stacks and the corresponding simulation results, which match well. The inset shows the definition of the switching time t_{SET}: For a rectangular voltage pulse with amplitude V_{app}—with a negligible rise time of 1 ns—the switching time t_{SET} is defined as the time between the start of the pulse and the current response at around 20% of the maximum current I_{max}, which is similar to the definition in measurements. For this sets of simulations, nanotemplates with a radius equal to 60% of the height of the oxide have been assumed, resulting in 6 nm for SiO_2 and 1.8 nm for HfO_2. The highly non-linear kinetics over many orders of magnitude match also the different limiting regimes, namely nucleation limitation (I), electron-exchange limitation (II) and the electron-exchange and ion drift limitation, also called mixed regime (III). While the transition from I to II is clearly recognizable by a change in slope, the transition from II to III is smooth. This marking is therefore only to be understood as approximate transition marking. The marked points (A–D) indicate identical filament morphologies of both simulated cell stacks. These morphologies are shown in figures 4(f)–(i) and will be discussed in detail later. Each subplot shows the evolution of CF morphologies over time, from 10% maximum height over 50%–97%, from dark to bright regions. Only the envelope is shown. The continuum modeling approach yields a limited number of possible CF morphologies for both sets of simulations. Therefore, the morphologies are normalized to the height of the SL. For a better comparison of the CF morphologies, two new sets of simulations will be introduced at this point, one for each cell stack. The morphologies of these sets will be discussed first and then compared to the originally introduced sets of simulations. The difference from the originally introduced two sets is that for the new sets of simulations, mechanical stress is set to zero while all other parameters remain identical. The resulting simulated kinetic curves remain unchanged, and generally no influence of the mechanical stress on the kinetics above the numerical noise level was found. However, the CF morphologies differ drastically. Without mechanical stress the morphology changes with the applied voltage from an isotropic and hemisphere-shaped CF (figure 4(a) SiO_2 0.2 V/HfO_2 0.4 V & 4(b) SiO_2 1.4 V/HfO_2 1.2 V) to a more anisotropic and directed grown CF (figure 4(c) SiO_2 2.0 V/HfO_2 1.8 V). For the highest voltage (SiO_2 2.5 V/HfO_2 2.2 V), a cone-shaped CF grows (figure 4(d)). The reason for the directed growth is a significant voltage drop in the SL. A significant voltage drop across the SL means that the ionic current density becomes inhomogeneous within the SL. Higher electric fields at the CF tip lead to ionic current crowding at this location and reduction of the ionic current at the CF/CE interface. This effect leads to directed CF growth, which is proportional to the local ionic current density. If the voltage is further increased, the electric field elevation at the tip of the CF increases the ion injection in the SL and the ionic conductivity such that thin, dendritic-like growth can be observed. The threshold for this kind of growth mode lies at an electric field of $E \geqslant 100$ MVm^{-1} at the CF tip, where the maximum is always located. Figure 4(e) shows a CF, where the tip of the CF starts growing infinitesimal thin and the inset shows a zoom on the pinched tip. As a result of the pinching, the numerical element sizes converge to zero and the simulation aborts at this point. A further increase of the applied voltage shifts the start of this growth mode to earlier times in the simulation, and thus aborting the simulation before the CF reaches 97% of the SL thickness. Figure 4(e) shows the last successful simulation

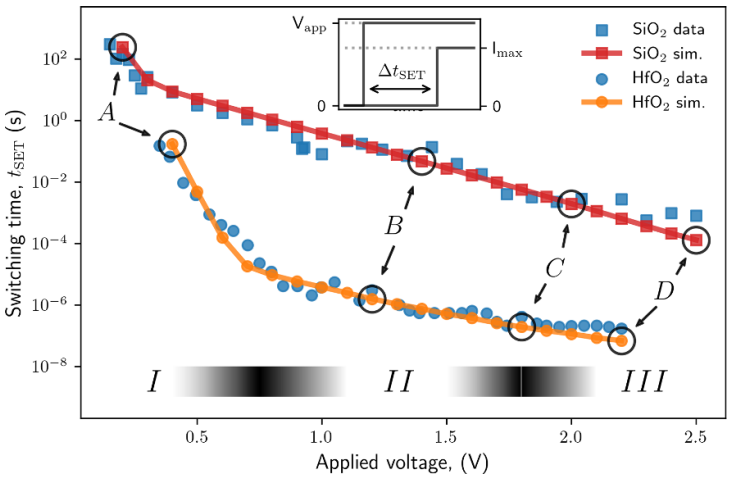

Figure 3. Simulation results in good agreement with experimental data for non-volatile Ag/SiO_2/Pt cells [64] and volatile Ag/HfO_2/Pt cells [26]; marked points A,B,C,D show similar CF morphologies; the inset shows electrical stimulus and definition of t_{SET}, experimental data only shows the mean values.

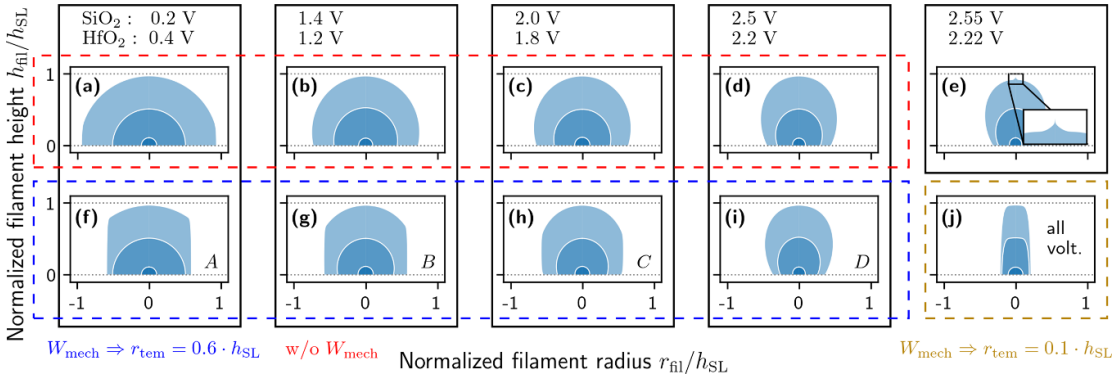

Figure 4. Simulated CF morphology and evolution over time is displayed from 10% maximum height over 50%–97% height (dark to bright regions) and only the envelopes are shown; (a)–(e) CFs w/o mechanical stress with increasing voltage; (f)–(i) CFs with mechanical stress and increasing voltage, corresponding to the curves and marked points in figure 3, the nanotemplate is wider than the smallest CF w/o mechanical stress; (j) wire-like CF due to small nanotemplate, independent of applied voltage. Note that the CF morphologies are normalized to the SL height, as the morphologies are identical for the simulated material systems. Gray dotted lines within the subplots at top and bottom of the CFs indicate AE/SL and SL/CE interfaces.

before this effect applies. In numbers for the SiO_2 /HfO_2 stack this means increasing the voltage from (d) 2.5 V/2.2 V to (e) 2.55 V/2.22 V.

The CFs without mechanical stress are directional, but still quite bulky and contradict various CF observations in solid SLs [20, 29–32], but fit quite well CF observations in Ag/H_2O/Pt cells, with liquid water as SL [33]. The difference between solid and liquid SLs is that for the former it can be expected that CF growth induces mechanical stress, which should constrain the CFs lateral dimension, while for the latter the ions can move freely. In fact, by adding mechanical stress to the model, different constraints on the CF morphology can be observed, depending on the size of the nanotemplate. Two meaningful cases can be identified: a nanotemplate equal or larger than the widest CF radius in figure 4(d) and a nanotemplate smaller than this radius. The first case is of interest, as it shows that mechanical stress could be neglected to explain CF morphologies at higher voltages. The first case was assumed in the originally introduced sets of simulations with a nanotemplate of $r_{tem} = 0.6\ h_{SL}$. Now the CF morphologies of these sets of simulations will be discussed and compared. Mechanical stress suppresses lateral growth beyond the nanotemplate. Thus, the resulting CF morphologies are laterally constraint for a part of the observed voltage range (figures 4(f)–(h)). The former hemisphere-shaped CFs are still bulky, but now they are cylindrical and have a narrowed tip. With increasing voltage, the CF morphologies become directional and the explanations for directed growth hold for this type of simulations. At the highest applied voltage (figure 4(i), SiO_2 2.5 V/HfO_2 2.2 V), the CF morphology is so directional, that the CF only grows within the nanotemplate and thus, is unaffected by mechanical stress. Consequently, the CF morphologies in figures 4(d) and (i) are identical. These CF

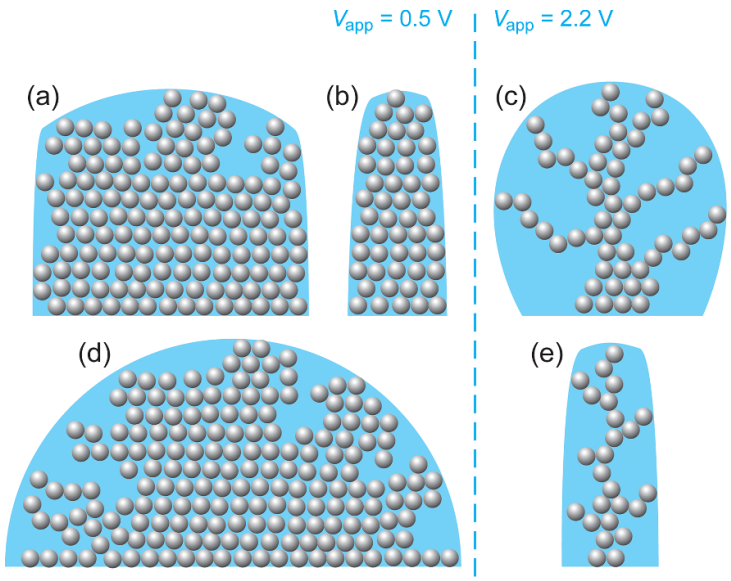

Figure 5. Schematic representation of the inner structure of simulated CF morphologies with and without mechanical stress at high and low voltages. (a) $V_{app} = 0.5$ V, $r_{tem} = 0.6\ h_{SL}$, (b) $V_{app} = 0.5$ V, $r_{tem} = 0.1\ h_{SL}$, (c) $V_{app} = 2.2$ V, without mechanical stress, (d) $V_{app} = 0.5$ V, no mechanical stress, (e) $V_{app} = 2.2$ V, $r_{tem} = 0.1\ h_{SL}$; the spheres represent Ag atoms.

morphologies fit well various *in situ* (HR) TEM observations of bulky and directed cone-shaped CFs [20, 29–32]. The best agreement with these observations was obtained by performing another set of simulations for both material systems with a nanotemplate corresponding to the afore mentioned second case, giving $r_{tem} = 1$ nm for SiO_2 and $r_{tem} = 0.3$ nm for HfO_2. The resulting CF morphology is displayed in figure 4(j), a thin cylindrical wire. The unique feature of this set of simulations is that the morphology is determined solely by the mechanical stress and no longer depends on the applied voltage.

The internal structure of the observed CFs varies from dense and solid grown to coarse and dendritic grown with respect to the density of the metal atoms within the CF domain. To address this issue, figure 5 shows the possible atomic configuration of different simulated CF morphologies. A solid and dense atomic structure can be expected at lower voltages, with (figures 5(a) and (b)) and without mechanical stress (figure 5(d)). For higher applied voltages and thus directed growth—due to the formerly explained voltage drop effect within the SL (figure 5(c)) or mechanical stress (figure 5(e))—a coarse and dendritic configuration could be expected. Our model cannot simulate those internal atomic structures due to its continuous approach. The spheres depict metal atoms that form different configurations during growth as function of the model parameter.

The effective radius of the CFs, shown in figure 5, allows conclusions to be drawn about retention. A thicker and denser CF (figures 5(a) and (b)) should have a higher retention than a thin dendritic CF (figures 5(c) and (e)) [26, 65]. Consequently, depending on the application, the retention can be adjusted via the applied voltage. However, it should be noted that not only the applied voltage, but also the maximum current and the duration of the pulse after t_{SET} play a role, which can lead to a contact of the CF with the AE depending on the bias. This cannot be described by the present model and offers a starting point for future studies.

3.2. Influence of the ionic conductivity

In this section, the influence of the ionic conductivity on the kinetics and the CF morphology will be discussed. Two sets of kinetic simulations with increased ionic conductivity were performed, one for a SiO_2 stack and one for a HfO_2 stack. For both sets of simulations, the parameters from tables 1 and 2 were applied, but the ionic conductivity σ_{ion} from equation (3) was multiplied with a factor of 10 and 100, respectively. Mechanical stress was neglected. For better comparison with the simulation results from figure 3, denoted as $t_{SET,0}$, the new results where normalized to $t_{SET,0}$. The resulting increase of the switching time t_{SET} is shown in figure 6. It was found that the increase of the ionic conductivity σ_{ion} leads to higher SET time t_{SET} ($\hat{=}$ slower switching) in the electron transfer (II) and mixed regimes (III). For SiO_2 and HfO_2 the maximum increase of switching time is about 25% and 34%, respectively. In comparison to the variability of the kinetic measurements, this is small [26, 64]. The trend that higher ionic conductivity leads to higher SET times, matches experimental findings, where kinetic measurements with different doping concentrations of mobile

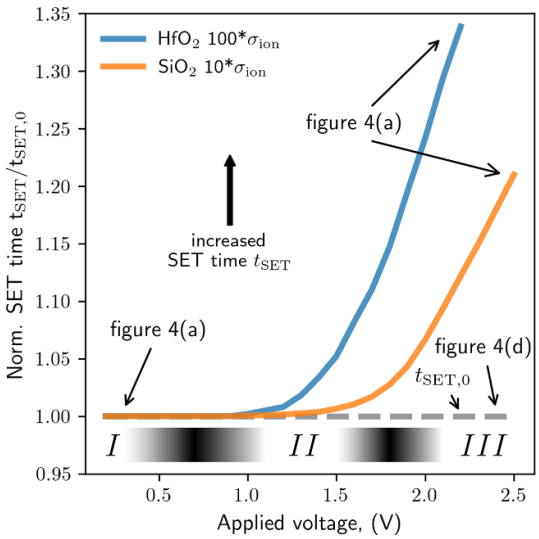

Figure 6. SET time with increased ionic conductivity normalized to values from figure 3. The increase of ionic conductivity leads to higher SET times at intermediate and high applied voltages in the electron exchange (II) and mixed regimes (III). Only isotropic hemisphere-shaped CF growth is observed, due to increased ionic conductivity σ_{ion}. CF morphologies are linked to figure 4.

ions in the SL have been reported. Higher doping of mobile ions and thus higher ionic conductivity of the SL leads to higher SET times [66, 67]. The reason for the higher SET time with higher ionic conductivity is counterintuitive. It would be expected that higher ionic conductivity would lead to higher ionic currents and thus faster growth of the CF and lower SET times. In fact, the higher ionic conductivity leads to a more homogeneous current density within the SL, which leads to isotropic hemisphere-shaped CF growth (figure 4(a)). In contrast, a reduced ionic conductivity leads to current crowding at the CF tip, due to the voltage drop within the SL. The result is an increased ionic current density at the CF tip, leading to an anisotropic cone-shaped CF (figure 4(d)). From equation (10) follows directly that the increased current density at the CF tip leads to increased vertical growth speed of the CF and thus lower SET time. If follows that by adjusting the ionic conductivity the CF morphology can be adjusted along the applied voltage range. The parameters in tables 1 and 2 were adjusted to produce the thinnest possible CF at the highest simulated voltages for SiO_2 and HfO_2, respectively.

However, an increased ionic conductivity of the SL also leads to a change in the voltage drop across the cell stack due to the series resistance. For the Ag/HfO_2/Pt cell stack, the voltage is reduced by about 40 mV when the ionic conductivity of the SL is increased by a factor of 100. This is not sufficient to explain the slower switching. To support our claim, the ionic current density along the CF/SL interface is shown in figure 7 for the Ag/HfO_2/Pt cell stack. The applied voltage was 2 V and the time of the ionic current density shown corresponds to a CF height of 1.5 nm, i.e. 50% of the SL thickness. It should be mentioned that the ionic current density shown in figure 7 is only a snapshot and is not constant over time. The ratio of the maxima also changes over time, but on average, the ionic current density remains higher for the unchanged ionic conductivity.

3.3. Influence of the Young's modulus

To qualify the influence of the Young's modulus Y on the CF morphology, a new set of simulations is performed, one each for the SiO_2 stack and the HfO_2 stack. Each set was simulated with the parameters from tables 1 and 2. The applied voltage was 0.2 V for SiO_2 and 0.4 V for HfO_2 and the size of the nanotemplate $r_{\text{TEM}} = 1/6\ h_{\text{SL}}$. The Young's modulus was varied between 0 and 180 GPa and for each variation the maximum lateral and vertical CF dimension was extracted at each time step.

The extracted results were normalized to the height of the SL h_{SL} in the specific simulations. Since the normalized results from SiO_2 and HfO_2 are indistinguishable, the results can be seen as generalized results, characterizing the simulation model. Figure 8 shows the normalized vertical CF dimension vs. the normalized lateral CF dimension for different Young's moduli. The time increases along the graphs, starting at $t = 0$ at the bottom and increasing towards the top. The dashed line indicates the exemplary nanotemplate equal to 1/6 h_{SL}. For 0 GPa no mechanical stress occurs and consequently an isotropic and hemisphere-shaped CF grows, indicated by the gray plot line with a slope of 1. For Young's moduli >0 GPa, the CF gets laterally constraint, leading to anisotropic cone-shaped CFs. For high Young's moduli ($\geqslant$60 GPa) only minimal overgrowth occurs, resulting in a well-defined CF morphology depending on the size of the

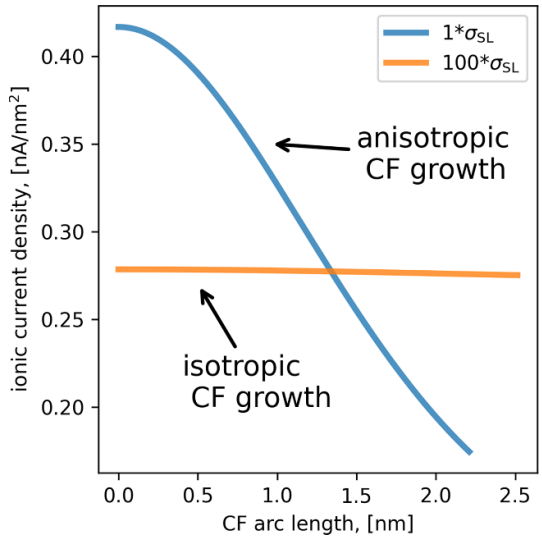

Figure 7. Ionic current density along the CF boundary of an Ag/HfO_2 (3 nm)/Pt cell for an applied voltage of 2 V and a CF height of 1.5 nm. If the ionic conductivity is increased by a factor of 100, the ion current density along the CF becomes almost constant, resulting in isotropic CF growth and slower switching, in contrast to the unadjusted ionic conductivity.

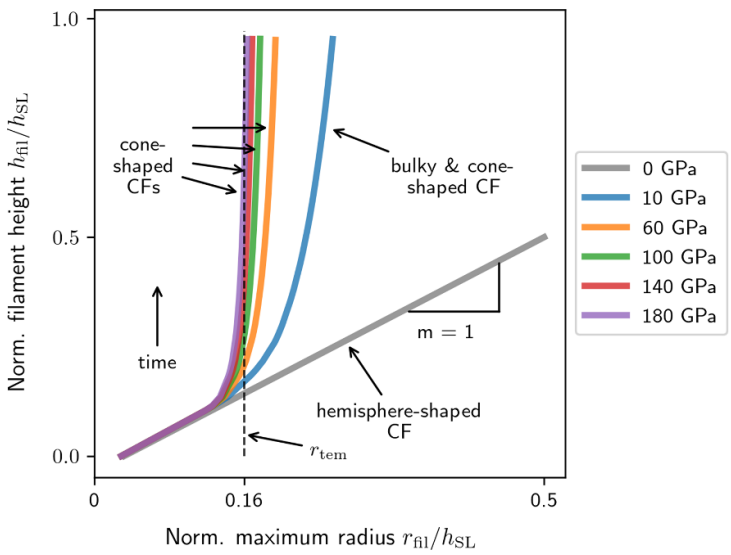

Figure 8. Vertical vs lateral CF growth and influence of different Young's moduli on the lateral CF dimension. Time increases from bottom to top. The gray graph has a slope of $m = 1$ and therefore exhibits isotropic growth, while the others graphs show anisotropic growth in vertical direction. The applied voltage was 0.2 V for SiO_2 and 0.4 V for HfO_2 and the size of the nanotemplate $r_{TEM} = 1/6\ h_{SL}$. The normalized results for both stacks coincide.

nanotemplate. The CF significantly overgrows the nanotemplate for values $\leqslant$10 GPa, because the additionally induced energy barrier for reduction is too low to hinder lateral CF growth. The comparison between the influence of the size of the nanotemplate and Young's modulus shows that the size of the nanotemplate has significant influence on the CF morphology, while the Young's modulus only needs to reach a certain threshold value to limit CF growth to the nanotemplate domain.

3.4. Discussion

The lifetime of a CF in non-volatile and volatile ECM cells is often linked to the radius r_{fil} of the CF [18, 24–27]. In experiments, the self-relaxation time t_r of volatile ECM cells decreases with increased SET voltage. According to Herrings scaling law ($t_r \propto r_{fil}^4$), experimental data can be explained if the CF radius changes by one order of magnitude across the applied voltage range. Without mechanical stress, almost a factor of two was achieved in CF radius reduction between lowest and highest applied voltage. With mechanical stress, it is possible to achieve a reduction of up to one order of magnitude, depending on the size of the nanotemplate. However, the downside of small nanotemplates is the loss of voltage dependency on the CF morphology. For

volatile ECM cells and in the context of the present model, it would therefore be reasonable to assume nanotemplates large enough not to suppress the voltage dependence.

The doping of the SL is reported to have a major influence on the retention of non-volatile ECM cells [67]. In the present model it was shown that ionic conductivity can be linked to doping in real ECM cells. It was found, that higher conductivity leads to bigger, bulkier CFs, which might be more stable and therefore can explain retention effects in non-volatile ECM cells.

4. Conclusion

We presented a 2D axisymmetric continuum model for the SET kinetics in volatile and non-volatile ECM cells. The model accurately matches the kinetic measurements and predicts different, in experiments *in situ* observed CF morphologies. The concentration of mobile ions was identified as a critical parameter to establish a voltage dependency of the CF morphology. The concentration of mobile ions and thus the ionic conductivity has to be low enough to cause a significant voltage drop in the insulator at medium and higher voltages. As a result, current crowding occurs at the tip and anisotropic, directional, cone-shaped CFs grow. At low voltages, the voltage drop should be so low that no significant current crowding occurs at the CF tip. This results in hemisphere-shaped CFs. This CFs have to be laterally confined to match observations in experiments. This was achieved by implementing mechanical stress. Depending on the size of the nanotemplate, in which the CF can grow unhindered, different CF morphologies occur. Small nanotemplates lead to directed, wire-like CFs, which are independent of the applied voltage and wide nanotemplates lead to bulky filaments. At high voltages a directed, cone-shaped CF can grow within the wider nanotemplates, independent of the mechanical stress. A reduction of the filament radius of a factor of $\sim$2 was achieved within the investigated voltage range without mechanical stress. With mechanical stress, the radius can be further decreased up to a factor of 10. It was also shown, that the ionic conductivity of the SL influences the morphology and SET time. The resulting change in CF diameter—from mechanical stress or ionic conductivity—can be used to explain retention and self-relaxation processes in volatile and non-volatile ECM cells. The results provide information to develop more reliable volatile and non-volatile ECM cells and therefore pave the way for neuromorphic computing and applications as selector or memory device. Regarding the influence of doping concentration of mobile ions, i.e. ionic conductivity, the results also raise open questions that may guide future experiments.

Data availability statement

The data cannot be made publicly available upon publication because they are not available in a format that is sufficiently accessible or reusable by other researchers. The data that support the findings of this study are available upon reasonable request from the authors.

Acknowledgments

This work was partially supported by the European project MEMQuD, code 20FUN06. by the EMPIR programme cofinanced by the Participating States and from the European Union's Horizon 2020 research and innovation programme, part by the Deutsche Forschungsgemeinschaft (DFG) under Grant SFB 917, in part by the German Federal Ministry of Education and Research (BMBF for its initials in German) through the projects 'Neuro-inspired Artificial Intelligence Technologies for the Electronics of the Future' (NEUROTEC) under Projects 16ME0398K and 16ME0399,

ORCID iDs

Milan Buttberg https://orcid.org/0000-0003-1647-4254
Ilia Valov https://orcid.org/0000-0002-0728-7214

References

[1] Meena J S, Sze S M, Chand U and Tseng T-Y 2014 Overview of emerging nonvolatile memory *Nanoscale Res. Lett.* **9** 1–33
[2] Hirose Y and Hirose H 1976 Polarity-dependent memory switching and behaviour of Ag dendrite in Ag-photodoped amorphous As_2S_3 films *J. Appl. Phys.* **47** 2767–72
[3] Kozicki M N, Yun M, Hilt L and Singh A 1999 Applications of programmable resistance changes in metal-doped chalcogenides *Electrochem. Soc.* **298** 309
[4] Kund M, Beitel G, Pinnow C U, Roehr T, Schumann J, Symanczyk R, Ufert K D and Mueller G 2005 Conductive bridging RAM (CBRAM): an emerging non-volatile memory technology scalable to sub 20 nm *IEDM Technical Digest* pp 754–7

[5] Menzel S 2017 Comprehensive modeling of electrochemical metallization memory cells (online first) *J. Comput. Electron.* **16** 1017–37
[6] Abbas H, Li J and Ang D S 2022 Conductive bridge random access memory (CBRAM): challenges and opportunities for memory and neuromorphic computing applications *Micromachines* **13** 725
[7] Ielmini D and Waser R 2016 *Resistive Switching—From Fundamentals of Nanoionic Redox Processes to Memristive Device Applications* (Weinheim: Wiley-VCH) (https://doi.org/10.1002/9783527680870)
[8] Lee T S, Lee N J, Abbas H, Lee H H, Yoon T-S and Kang C J 2020 Compliance current-controlled conducting filament formation in tantalum oxide-based RRAM devices with different top electrodes *ACS Appl. Electron. Mater.* **2** 1154–61
[9] Ali A, Abbas H, Hussain M, Hassan Abbas Jaffery S, Hussain S, Choi C and Jung J 2022 Thickness-dependent monochalcogenide GeSe-based CBRAM for memory and artificial electronic synapses *Nano Res.* **15** 1–15
[10] Pan C *et al* 2017 Coexistence of grain-boundaries-assisted bipolar and threshold resistive switching in multilayer hexagonal boron nitride *Adv. Funct. Mater.* **27** 1604811/1–10
[11] Hussain T *et al* 2022 Cellulose nanocrystal based bio-memristor as a green artificial synaptic device for neuromorphic computing applications *Adv. Mater. Technol.* **7** 2100744
[12] Waser R, Dittmann R, Staikov G and Szot K 2009 Redox-based resistive switching memories—nanoionic mechanisms, prospects, and challenges *Adv. Mater.* **21** 2632–63
[13] Terabe K, Hasegawa T, Nakayama T and Aono M 2005 Quantized conductance atomic switch *Nature* **433** 47–50
[14] Tappertzhofen S, Valov I and Waser R 2012 Quantum conductance of AgI based resistive switches: towards an atomic scale memory *Nature Conf.* pp 208–9
[15] Milano G, Boarino L, Valov I and Ricciardi C 2022 Memristive devices based on single ZnO nanowires—from material synthesis to neuromorphic functionalities *Semicond. Sci. Technol.* **37** 034002
[16] Schindler C 2009 Resistive switching in electrochemical metallization memory cells *Doctoral Dissertation* RWTH Aachen
[17] Chekol S A, Cüppers F, Waser R and Hoffmann-Eifert S 2021 An Ag/HfO_2/Pt threshold switching device with an ultra-low leakage (<10 fA), high on/off ratio (>1011), and low threshold voltage (<0.2 V) for energy-efficient neuromorphic computing *2021 IEEE Int. Memory Workshop (IMW)* (IEEE) pp 1–4
[18] Wang W, Wang M, Ambrosi E, Bricalli A, Laudato M, Sun Z, Chen X and Ielmini D 2019 Surface diffusion-limited lifetime of silver and copper nanofilaments in resistive switching devices *Nat. Commun.* **10** 81
[19] Chen W, Fang R, Balaban M B, Yu W, Gonzalez-Velo Y, Barnaby H J and Kozicki M N 2016 A CMOS-compatible electronic synapse device based on Cu/SiO_2/W programmable metallization cells *Nanotechnology* **27** 255202/1–9
[20] Wang Z *et al* 2017 Memristors with diffusive dynamics as synaptic emulators for neuromorphic computing *Nat. Mater.* **16** 101–8
[21] Zhuo Y *et al* 2021 A dynamical compact model of diffusive and drift memristors for neuromorphic computing *Adv. Electron. Mater.* **8** 2100696
[22] Wang Z *et al* 2018 Fully memristive neural networks for pattern classification with unsupervised learning *Nat. Electron.* **1** 137–45
[23] Yeon H *et al* 2020 Alloying conducting channels for reliable neuromorphic computing *Nat. Nanotechnol.* **15** 574–9
[24] Wang Y, Yu H and Zhang W 2014 Nonvolatile CBRAM-crossbar-based 3-D-integrated hybrid memory for data retention *IEEE Trans. Very Large Scale Integr. VLSI Syst.* **22** 957–70
[25] Zhao Y, Huang P, Zhou Z, Li C, Qin S, Liu L, Liu X, Philip Wong H S and Kang J 2019 A physics-based compact model for CBRAM retention behaviors based on atom transport dynamics and percolation theory *IEEE Electron Device Lett.* **40** 647–50
[26] Chekol S A, Menzel S, Ahmad R W, Waser R and Hoffmann-Eifert S 2022 Effect of the threshold kinetics on the filament relaxation behavior of Ag-based diffusive memristors *Adv. Funct. Mater.* **32** 2111242/1–11
[27] Guy J *et al* 2013 Investigation of the physical mechanisms governing data-retention in down to 10nm nano-trench Al_2O_3/CuTeGe conductive bridge RAM (CBRAM) *Electron Devices Meeting (IEDM), 2013 IEEE Int.* pp 30.2.1–30.2.4
[28] Celano U *et al* 2014 Three-dimensional observation of the conductive filament in nanoscaled resistive memory devices *Nano Lett.* **14** 2401–6
[29] Yang Y, Gao P, Gaba S, Chang T, Pan X and Lu W 2012 Observation of conducting filament growth in nanoscale resistive memories *Nat. Commun.* **3** 732
[30] Takahashi Y, Kudo M, Fujiwara I, Shimuta M, Ohba K and Arita M 2015 Visualization of conductive filament during write and erase cycles on nanometer-scale ReRAM achieved by *in-situ* TEM *2015 IEEE International Memory Workshop (IMW)* pp 1–4
[31] Yuan F, Zhang Z, Liu C, Zhou F, Yau H M, Lu W, Qiu X, Wong H-S P, Dai J and Chai Y 2017 Real-time observation of the electrode-size-dependent evolution dynamics of the conducting filaments in a SiO_2 layer *ACS Nano* **11** 4097–104
[32] Sun H, Liu Q, Li C, Long S, Lv H, Bi C, Huo Z, Li L and Liu M 2014 Direct observation of conversion between threshold switching and memory switching induced by conductive filament morphology *Adv. Funct. Mater.* **24** 5679–86
[33] Guo X, Schindler C, Menzel S and Waser R 2007 Understanding the switching-off mechanism in Ag^+ migration based resistively switching model systems *Appl. Phys. Lett.* **91** 1–3
[34] Rajabi S, Saremi M, Barnaby H, Edwards A, Kozicki M, Mitkova M, Mahalanabis D, Gonzalez-Velo Y and Mahmud A 2015 Static impedance behavior of programmable metallization cells *Solid State Electron.* **106** 27–33
[35] Belmonte A, Celano U, Redolfi A, Fantini A, Muller R, Vandervorst W, Houssa M, Jurczak M and Goux L 2015 Analysis of the excellent memory disturb characteristics of a hourglass-shaped filament in Al_2O_3/Cu-based CBRAM devices *IEEE Trans. Electron Devices* **62** 2007–13
[36] Menzel S, Adler N, van den Hurk J, Tappertzhofen S, Valov I and Waser R 2013 Simulation of polarity independent RESET in electrochemical metallization memory cells *2013 5th IEEE Int. Memory Workshop (IMW)* (*Taipeh, Taiwan, 26–29 May 2013*) pp 92–95
[37] Lv S, Liu J, Sun L, Wang H, Zhang J and Yu Z 2013 An analytical model for predicting forming/switching time in conductive-bridge resistive random-access memory (CBRAM) *2013 Int. Conf. on Simulation of Semiconductor Processes and Devices (SISPAD)* pp 364–7
[38] Ielmini D, Balatti S and Larentis S 2013 Filament evolution during set and reset transitions in oxide resistive switching memory *Jpn. J. Appl. Phys.* **52** 04CD10
[39] Bousoulas P, Sakellaropoulos D, Papakonstantinopoulos C, Kitsios S, Arvanitis C, Bagakis E and Tsoukalas D 2020 Investigating the origins of ultra-short relaxation times of silver filaments in forming-free SiO_2-based conductive bridge memristors *Nanotechnology* **31** 454002
[40] Guy J *et al* 2015 Investigation of forming, SET, and data retention of conductive-bridge random-access memory for stack optimization *IEEE Trans. Electron Devices* **62** 3482–9

[41] Menzel S, Kaupmann P and Waser R 2015 Understanding filamentary growth in electrochemical metallization memory cells using kinetic Monte Carlo simulations *Nanoscale* **7** 12673–81
[42] Qin S, Liu Z, Zhang G, Zhang J, Sun Y, Wu H, Qian H and Yu Z 2015 Atomistic study of dynamics for metallic filament growth in conductive-bridge random access memory *Phys. Chem. Chem. Phys.* **17** 8627–32
[43] Ambrogio S, Balatti S, Choi S and Ielmini D 2014 Impact of the mechanical stress on switching characteristics of electrochemical resistive memory *Adv. Mater.* **26** 3885–92
[44] Yang Y, Gao P, Li L, Pan X, Tappertzhofen S, Choi S, Waser R, Valov I and Lu W D 2014 Electrochemical dynamics of nanoscale metallic inclusions in dielectrics *Nat. Commun.* **5** 4232/1–9
[45] O'Dwyer J J 1973 *The Theory of Electrical Conduction and Breakdown in Solid Dielectrics* (Oxford: Clarendon)
[46] Mott N F and Gurney R W 1948 *Electronic Processes in Ionic Crystals* (London: Oxford University Press)
[47] Hamann C H, Hamnett A and Vielstich W 2007 *Electrochemistry* (Weinheim: Wiley-VCH)
[48] Dickinson E J F and Wain A J 2020 The Butler-Volmer equation in electrochemical theory: origins, value, and practical application *J. Electroanal. Chem.* **872** 114145
[49] Simmons J G 1963 Low-voltage current-voltage relationship of tunnel junctions *J. Appl. Phys.* **34** 238–9
[50] Matthews N, Hagmann M J and Mayer A 2018 Comment: "Generalized formula for the electric tunnel effect between similar electrodes separated by a thin insulating film" *J. Appl. Phys.* **123** 1793
[51] Menzel S 2012 Modeling and simulation of resistive switching devices RWTH Aachen
[52] Valov I, Sapezanskaia I, Nayak A, Tsuruoka T, Bredow T, Hasegawa T, Staikov G, Aono M and Waser R 2012 Atomically controlled electrochemical nucleation at superionic solid electrolyte surfaces *Nat. Mater.* **11** 530–5
[53] Lu Y M, Noman M, Chen W, Salvador P A, Bain J A and Skowronski M 2012 Elimination of high transient currents and electrode damage during electroformation of TiO_2-based resistive switching devices *J. Phys. D: Appl. Phys.* **45** 395101
[54] Hennen T, Wichmann E, Elias A, Lille J, Mosendz O, Waser R, Wouters D J and Bedau D 2021 Current-limiting amplifier for high speed measurement of resistive switching data *Rev. Sci. Instrum.* **92** 054701
[55] Li Y, Zhang L J, Cui T, Li Y W, Wang Y, Ma Y M and Zou G T 2008 First-principles studies of phonon instabilities in AgI under high pressure *J. Phys.: Condens. Matter* **20** 195218
[56] Kudelka R, Vaclavek L and Tomastik J 2016 Laser-induced surface acoustic waves for thin film characterization *Acta Polytech. CTU Proc.* **27** 57–61
[57] Vargas A L M, de Araújo Ribeiro F and Hübler R 2015 Changes in the Young Modulus of hafnium oxide thin films *Nucl. Instrum. Methods Phys. Res.* **365** 362–6
[58] Menzel S, Tappertzhofen S, Waser R and Valov I 2013 Switching kinetics of electrochemical metallization memory cells *Phys. Chem. Chem. Phys.* **15** 6945–52
[59] Waser R (ed) 2012 *Nanoelectronics and Information Technology* (Berlin: Wiley)
[60] Nayak A, Tamura T, Tsuruoka T, Terabe K, Hosaka S, Hasegawa T and Aono M 2010 Rate-limiting processes determining the switching time in a Ag_2S atomic switch *J. Phys. Chem. Lett.* **1** 604–8
[61] Tsuruoka T, Hasegawa T, Valov I, Waser R and Aono M 2013 Rate-limiting processes in the fast SET operation of a gapless-type Cu-Ta_2O_5 atomic switch *AIP Adv.* **3** 32114
[62] Kozicki M N and Barnaby H J 2016 Conductive bridging random access memory-materials, devices and applications *Semicond. Sci. Technol.* **31** 113001
[63] Chekol S A, Menzel S, Waser R and Hoffmann-Eifert S 2022 Strategies to control the relaxation kinetics of Ag-based diffusive memristors and implications for device operation *Adv. Electron. Mater.* **8** 2200549/1–11
[64] Luebben M, Menzel S, Park S G, Yang M, Waser R and Valov I 2017 SET kinetics of electrochemical metallization cells—influence of counter electrodes in SiO_2/Ag based systems *Nanotechnology* **28** 135205
[65] Ielmini D, Nardi F, Cagli C and Lacaita A L 2010 Trade-off between data retention and reset in NiO RRAMS *2010 Int. Reliability Physics Symp.* pp 620–6
[66] Lübben M, Cüppers F, Mohr J, von Witzleben M, Breuer U, Waser R, Neumann C and Valov I 2020 Design of defect-chemical properties and device performance in memristive systems *Sci. Adv.* **6** eaaz9079
[67] Longnos F *et al* 2013 On the impact of Ag doping on performance and reliability of GeS2-based conductive bridge memories *Solid State Electron.* **84** 155–9